

# Ultraviolet Raman Wide-Field Hyperspectral Imaging Spectrometer for Standoff Trace Explosive Detection

Applied Spectroscopy  
2017, Vol. 71(2) 173–185  
© The Author(s) 2016  
Reprints and permissions:  
sagepub.co.uk/journalsPermissions.nav  
DOI: 10.1177/0003702816680002  
journals.sagepub.com/home/asp  


Kyle T. Hufziger, Sergei V. Bykov, and Sanford A. Asher

## Abstract

We constructed the first deep ultraviolet (UV) Raman standoff wide-field imaging spectrometer. Our novel deep UV imaging spectrometer utilizes a photonic crystal to select Raman spectral regions for detection. The photonic crystal is composed of highly charged, monodisperse  $35.5 \pm 2.9$  nm silica nanoparticles that self-assemble in solution to produce a face centered cubic crystalline colloidal array that Bragg diffracts a narrow  $\sim 1.0$  nm full width at half-maximum (FWHM) UV spectral region. We utilize this photonic crystal to select and image two different spectral regions containing resonance Raman bands of pentaerythritol tetranitrate (PETN) and  $\text{NH}_4\text{NO}_3$  (AN). These two deep UV Raman spectral regions diffracted were selected by angle tuning the photonic crystal. We utilized this imaging spectrometer to measure 229 nm excited UV Raman images containing  $\sim 10$ – $1000$   $\mu\text{g}/\text{cm}^2$  samples of solid PETN and AN on aluminum surfaces at 2.3 m standoff distances. We estimate detection limits of  $\sim 1$   $\mu\text{g}/\text{cm}^2$  for PETN and AN films under these experimental conditions.

## Keywords

Wide-field imaging, ultraviolet (UV) resonance Raman, explosive detection, standoff, photonic crystal, pentaerythritol tetranitrate, PETN, ammonium nitrate

Date received: 25 August 2016; accepted: 16 October 2016

## Introduction

The increasing use of explosive devices in terrorist attacks has dramatically increased the need for sensitive standoff explosive detection instruments that can be utilized to screen for trace explosive residues that may indicate the presence of explosive threats.<sup>1,2</sup> There is intense interest in detection of explosives at trace concentrations such as those present in explosive-laced fingerprints, on vehicle panels or other surfaces contaminated by explosive residues, and in vapors surrounding buried landmines.<sup>3–6</sup> Trace explosive detection is challenging because explosives typically have low vapor pressures, making vapor detection difficult.<sup>2,7</sup> In addition, explosives often quickly photolyze when exposed to near-ultraviolet (UV) irradiation from sunlight, as well as from deep UV irradiation during spectroscopic measurements.<sup>8–12</sup> Any detection methodology must be able to detect different classes of explosives that have widely varying chemical structures.

We have been developing deep UV resonance Raman spectroscopy for standoff trace explosive detection. We have determined deep UV Raman spectral signatures, cross-sections, and the UV photochemistry of many explosives.<sup>11–14</sup> We have also developed new spectroscopic

instrumentation, as well as novel, compact UV laser excitation sources.<sup>15</sup> We recently reviewed advances in UV Raman standoff methods and compared their utility to existing methodologies that are currently used to detect and screen for trace explosives.<sup>1</sup> These include canine olfaction, ion mobility spectrometry, fluorescence quenching devices, and colorimetric assays.<sup>16–18</sup> The key limitation of these other techniques is the necessity for humans, canines, or instrumentation to be in close proximity to the objects being screened. Laser-based spectroscopies are the only currently viable means to detect explosives from safe standoff distances.

Raman spectroscopy is an inelastic light scattering technique that is well suited for explosive detection because measured Raman spectra can serve as molecular fingerprints.<sup>14,19–21</sup> In a typical Raman measurement, a monochromatic excitation source, usually a focused laser,

---

Department of Chemistry, University of Pittsburgh, Pittsburgh, PA, USA

### Corresponding author:

Sanford Asher, 219 Parkman Ave, Chevron Science Center, Pittsburgh, Pennsylvania, 15260, United States.  
Email: asher@pitt.edu

excites a small area of a sample. The vibrational modes of molecules in the sample inelastically scatter Raman light, which is shifted from the excitation frequency by the frequency of the molecular vibration. The Raman scattered light is collected, dispersed by a spectrograph, and measured using a charge-coupled device (CCD) detector. Visible wavelength Raman spectroscopy has been previously used for standoff detection by exciting distant samples with a laser and collecting the Raman scattered light with a telescope.<sup>22,23</sup>

Raman imaging methodologies have also been utilized to characterize the spatial chemical composition of sample surfaces.<sup>24</sup> Raman imaging instruments can be broadly differentiated by whether they involve raster-scanning or wide-field illumination.<sup>25</sup> Raster-scan Raman imaging instruments typically either translate a focused laser and collection optics across a stationary sample or utilize scanning stages that precisely move the sample in front of a stationary focused laser. Raman spectra are measured at discrete points on the sample utilizing a traditional Raman spectrometer.<sup>26</sup> The collected spectra can be assembled to produce a hyperspectral Raman image that depicts the Raman spectra of the sample as a function of position.<sup>27</sup>

In cases where the available laser beam power is not limiting, wide-field imaging instruments can provide hyperspectral images with dramatically increased signal-to-noise (S/N) compared to raster-scan instruments.<sup>28</sup> In wide-field Raman instruments, a defocused laser beam illuminates a large region of the sample and the Raman scattered light is simultaneously collected from the entire illuminated area. The Raman scattered light is analyzed by a wavelength selection device (WSD) that selects a narrow wavelength spectral region of interest to form a wide-field Raman image of the entire sample surface. In the simplest case, the WSD selects a spectral region containing only a single Raman band of the analyte. In this case, the Raman image intensity details the spatial distribution of the analyte.<sup>29,30</sup>

Typically, the WSD is then tuned to image additional spectral regions, enabling the collection of a hyperspectral Raman image of the sample. In our previous work, we demonstrated the first use of a photonic crystal (PC) as a WSD to construct a visible wide-field imaging spectrometer with 488 nm excitation.<sup>29</sup> We pioneered and have extensively studied PCs composed of highly charged, self-assembling nanospheres that diffract light according to Bragg's Law.<sup>31,32</sup> We have utilized these PCs as visible Rayleigh rejection filters for Raman measurements and for numerous sensing applications including detection of small molecules, proteins, and micro-organisms.<sup>33–38</sup> Other groups have developed near-infrared (NIR) and visible wavelength Raman wide-field imaging spectrometers by utilizing liquid crystal tunable filters (LCTF), acousto-optic tunable filters (AOTF), and bandpass filter WSDs.<sup>26,39</sup>

Many previous standoff Raman explosive detection instruments utilized visible excitation due to the availability

of high performance visible optics and filters, efficient detectors, and high power visible laser sources.<sup>22,23,40,41</sup>

The major limitation of visible Raman for trace explosive detection derives from the weak Raman cross-sections that limit detection sensitivity. Furthermore, fluorescence caused by visible excitation can severely degrade Raman spectral S/N and visible excitation power must be severely constrained to maintain eye safety for detection in the field.

There is great interest in utilizing deep UV excitation for standoff explosive detection.<sup>1,15,42–44</sup> Deep UV excitation (<250 nm) has significant advantages for Raman standoff trace explosive detection. Raman scattering intensity has a  $\nu^4$  dependence on excitation frequency, yielding greater Raman intensities as the excitation wavelength decreases.<sup>20</sup> Excitation at <250 nm within the explosives' electronic absorption bands results in resonance Raman enhancements of up to  $10^6$ , significantly improving detection sensitivity.<sup>13,14,45</sup> Sample luminescence that notoriously degrades spectral S/N for visible and NIR Raman experiments occurs outside the Raman spectral region when deep UV excitation is utilized, improving sensitivity.<sup>46</sup> In addition, the ocular mean permissible exposure (MPE) set by ANSI for deep UV light is much higher than for visible excitation, enabling the use of higher laser power eye-safe deep UV instruments.<sup>47,48</sup> Thus, the sensitivity and selectivity of Raman instruments for explosive detection is dramatically increased for deep UV excitation, especially for trace samples likely to be encountered in the field.<sup>1,8,14,15,49</sup>

The primary challenge for deep UV wide-field imaging instrumentation is that until this work, there were no WSDs that functioned in the deep UV spectral region. We recently invented the first deep UV diffracting PC and demonstrated its use as a Rayleigh rejection filter for 229 nm UV Raman experiments.<sup>50</sup> We developed a modified Stöber synthesis to prepare highly charged, monodisperse  $\sim 47$  nm diameter silica nanoparticles. These particles self-assembled in solution to produce a PC that diffracted a narrow deep UV spectral region. We utilized this deep UV diffracting PC as a 229 nm Rayleigh rejection filter in a Raman measurement of Teflon, where the Stokes shifted Teflon Raman bands transmitted through the PC to be dispersed by the spectrograph. In the present work, we demonstrate the use of a silica nanoparticle PC as a WSD to construct the first deep UV standoff wide-field Raman imaging spectrometer for trace explosive detection.

## Experimental

### *Monodisperse Silica Nanoparticle Synthesis and Functionalization*

Monodisperse silica nanospheres were synthesized by using a scaled-up regrowth method first described by Hartlen et al.<sup>51</sup> Briefly, 99.5 mL nanopure H<sub>2</sub>O (Thermo Scientific Barnstead) was added to a jacketed 500 mL reactor

(Kontes) connected to an ethylene glycol bath (Thermo Scientific Neslab RTE 740) for temperature control. The reactor was fitted with a Teflon agitator (Ace Glass 8090-08) attached to an overhead stirrer (Caframo BDC6015) set to 60 RPM and a reflux condenser. 0.1825 g L-arginine (Sigma Aldrich A5006) was dissolved in 39.0 mL nanopure H<sub>2</sub>O and added to the reactor, followed by 12.0 mL cyclohexane (Fisher Scientific C556). After the reactor contents reached ~60 °C, 11.00 mL tetraethyl orthosilicate (TEOS, Sigma Aldrich 86578) was pipetted slowly down the reactor wall to prevent fast mixing with the aqueous layer, resulting in improved nanoparticle nucleation which increased the final particle monodispersity.<sup>51</sup> The reaction was allowed to proceed for 20 h before being cooled to room temperature. The resulting silica nanoparticle seed dispersion was  $24.7 \pm 2.8$  nm in diameter.

Between each synthesis step, the nanoparticle dispersion was removed and the reactor was washed with ethanol and nanopure H<sub>2</sub>O. To grow the silica nanoparticles to their final size, the entire nanoparticle seed dispersion was added to the reactor and stirring was restarted at 60 RPM. 490 mL nanopure H<sub>2</sub>O was added, followed by 53 mL cyclohexane. The recirculator heated the reactor to ~55 °C and 40.0 mL TEOS was pipetted slowly down the reactor wall. The reaction was allowed to proceed for 30 h before cooling to room temperature.

The resulting  $35.7 \pm 2.9$  nm nanoparticles were functionalized with 3-trihydroxysilyl-1-propane sulfonic acid (THOPS, Gelest SIT 8378.3) following a procedure described by Wang et al.<sup>50</sup> The entire dispersion was added to the reactor, stirring was restarted at 60 RPM, 100 mL nanopure H<sub>2</sub>O was added to the reactor, and the reactor heated to 70 °C. Approximately 4 mL NH<sub>4</sub>OH (Sigma Aldrich 21228) was added to 20.0 mL THOPS and the pH ~9 mixture was poured into the reactor. The reaction was allowed to proceed for 6 h before cooling to room temperature.

The dispersion was removed from the reactor and dialyzed (Sigma Aldrich D9652) against nanopure water for three days to remove unreacted species. Following dialysis, the dispersion was centrifuged at 18 000 g for at least 1 h, the supernatant was removed, and the pellet re-dispersed in nanopure H<sub>2</sub>O. Supernatant removal via centrifugation followed by redispersion was repeated four times before storing the final product over mixed bed ion exchange resin (Bio-Rad AG-501-X8 (D)) to remove any remaining ionic contaminants. The final nanoparticle size was measured to be  $35.5 \pm 2.9$  nm by TEM (Figure 1). We measured a  $\zeta$ -potential of -50.5 mV at pH 4.5.

### Nanoparticle and Photonic Crystal Diffraction Characterization

Nanoparticle sizes were measured by pipetting dilute dispersions onto Formvar coated copper grids (Ted Pella, 01814-F).

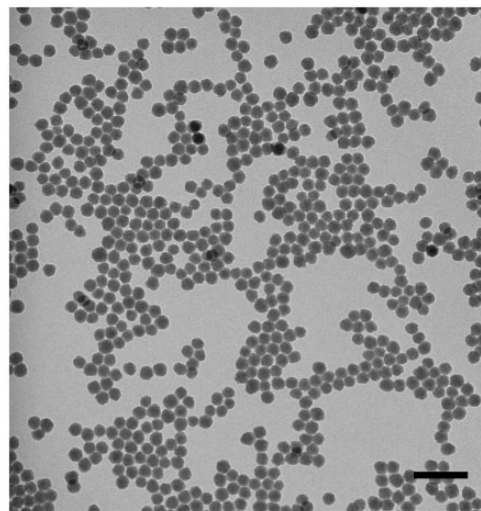


**Figure 1.** Transmission electron micrograph of highly charged  $35.5 \pm 2.9$  nm silica nanoparticles. Scale bar denotes 150 nm.

After air-drying, the grids were imaged using a transmission electron microscope (FEI Morgagni 268). At least 100 individual nanoparticles were measured via Image J (NIH)<sup>52</sup> to determine the particle size distribution. The  $\zeta$ -potential of a diluted nanoparticle dispersion was measured using dynamic light scattering (Malvern ZS-90 Zetasizer, Smoluchowski approximation). Sample pH was monitored during  $\zeta$ -potential measurements using pH strips (EMD Millipore ColorpHast 0–6 pH).

The transmission of UV light by the PC was monitored by using an ultraviolet–visible–near-infrared (UV-Vis-NIR) absorption spectrometer (Varian Cary 5000). The PC was held by a 2 in. mirror mount (Newport GM-2) attached to a rotational stage (Newport 481-A) mounted on a breadboard placed within the spectrometer. The PC diffraction bandwidth was directly determined by measuring the angular dependence of the power of a weak 229 nm laser beam diffracted by the PC. The PC was mounted to a rotational stage (Newport 481-A) and illuminated by ~150  $\mu$ W 229 nm continuous wave (CW) light generated by an intracavity frequency doubled Coherent Innova 300c FreD Ar ion laser.<sup>53</sup> The diffracted laser beam power was measured using a photodiode power meter (Thorlabs PM200 meter with a SI20VC head) and fit to a Gaussian for further analysis (OriginPro).

### Trace Explosive Sample Preparation

Drop-cast trace explosive samples were prepared on the surface of ~2.5 × 2.5 cm aluminum plates (McMaster-Carr, Multipurpose 6061 aluminum) that were first smoothed by a milling machine (Pitt Chemistry Machine Shop) followed by final polishing with fine grit sandpaper (Norton P800). The aluminum plates were thoroughly washed with

acetone, ethanol, and nanopure H<sub>2</sub>O before being dried with a stream of N<sub>2</sub>.

To prepare the drop-cast samples for Raman imaging, a 1.00 mL methanol solution containing 1.00 mg pentaerythritol tetranitrate (PETN, AccuStandard M-8330-ADD-2-10x) was evaporated using a gentle stream of N<sub>2</sub>. The small crystals were dissolved in 50.0 μL spectroscopic grade acetone (Acros 16764-5000, >99%). A total of 6.0 μL of a 20.0 mg/mL solution of NH<sub>4</sub>NO<sub>3</sub> (AN, EM Science AX1315-1, >99%) in spectroscopic grade methanol (Fisher Scientific A408-1, >99%) was drop-cast onto a section of a clean aluminum plate. A total of 6.0 μL of the PETN solution was drop-cast a short distance away. These droplets quickly evaporated to create two explosive films containing 760 μg/cm<sup>2</sup> AN and 920 μg/cm<sup>2</sup> PETN, respectively (Figure 6a and e). The total amount of explosive deposited in each film is 120 μg. Approximately 100 μg PETN and AN were similarly drop-cast onto two separate, clean aluminum plates for Raman spectral analysis (Figure 6b and f). Microscope images (DinoLite Edge) were recorded of the samples prior to irradiation.

It is well-known that solids migrate towards the edge of evaporating droplets, resulting in the formation of a “coffee-ring” where most of the solute becomes localized at the ring edge.<sup>54,55</sup> To increase film uniformity and surface coverage of these drop-cast explosive samples, we utilized high vapor pressure solvents and small solution volumes that were deposited in multiple aliquots with drying in between to minimize coffee-ring formation.

In addition to these drop-cast samples, we also measured 10, 100, and 250 μg/cm<sup>2</sup> PETN and AN inkjet printed explosive samples on smooth aluminum substrates (ACT Test Panel Technologies) donated by the US Army Research Lab (ARL). Preparation of these samples is described elsewhere.<sup>56</sup> Inkjet printing offers several important advantages over drop-cast deposition. Inkjet printing enables reproducible deposition of droplets that are several orders of magnitude smaller in volume than is possible using micropipettes, mitigating coffee ring formation.<sup>55</sup> Inkjet printing enables reproducible preparation of samples with well-defined explosive surface coverage via precise control of the volume, location, and number density of deposited droplets.

### Raman Measurements

Trace explosive samples were excited by 229 nm light generated by an intracavity doubled Ar ion laser, described above.<sup>53</sup> A custom deep UV optimized spectrometer (Spex Triplemate) equipped with a CCD (Roper Scientific Spec 10) was utilized to collect solid state deep UV Raman spectra of the explosives (Figure 6b and f).<sup>57</sup> The solid state explosive samples were illuminated by a ~4.3 mW, 229 nm beam with a ~70 μm spot size and were spun during irradiation (Figure 6b and f). Raman spectra were scaled

proportionally to the Raman cross-sections of their most intense Raman bands (1044 cm<sup>-1</sup> for NH<sub>4</sub>NO<sub>3</sub> and the sum of the 1269 + 1289 cm<sup>-1</sup> bands for PETN) after cosmic ray removal and calibration (Thermo GRAMS/AI 8.0) using solid state 229 nm Raman cross-sections measured by Emmons et al.<sup>49</sup>

For Raman imaging experiments, the 229 nm beam was directed through two plano-convex microlens arrays (Edmund Optics 64-477) to generate a square, ~1.2 × 1.2 cm beam at the sample. The total incident laser power was measured by a photodiode power meter (Thorlabs PM200 meter with a S120VC head) to be ~6.5 mW after the final turning mirror at the sample during the Raman imaging measurements.

All Raman images are depicted in false color by utilizing WinSpec software (Princeton Instruments). The false color contrast range that determines the color of each pixel in the Raman image was set to be identical for all Raman images with the same accumulation time (i.e., all 30 s Raman images have the same false color scale), enabling separate Raman images to be visually compared. Raman image false colors range from dark blue (low intensity) to bright red/white (high intensity). Laboratory lights were turned off during Raman image collection.

## Results and Discussion

### Photonic Crystal Diffraction

The low pK<sub>a</sub> sulfonic acid groups attached during THOPS functionalization of our monodisperse silica nanoparticles yields a high negative surface charge and a high ζ-potential of -50.5 mV at pH 4.5. We utilized these 35.5 ± 2.9 nm silica nanoparticles to fabricate PCs that diffract light in the deep UV spectral region (Figure 2). After thoroughly removing dissolved charged species from the nanoparticle dispersion, electrostatic repulsion between the highly charged nanoparticles caused self-assembly of a face centered cubic (FCC) crystal that diffracts light according to Bragg's Law (Eq. 1).<sup>29</sup>

$$m \lambda = 2 n d \sin \theta \quad (\text{Eq. 1})$$

where  $m$  is the diffraction order,  $\lambda$  is the wavelength of light in vacuum,  $n$  is the refractive index of the dispersion,  $d$  is the FCC ( $hkl$ ) plane spacing, and  $\theta$  is the glancing angle within the dispersion.<sup>58</sup> We utilize diffraction from the FCC (111) planes because their diffraction is highly spectrally separate from the higher Miller index planes. The FCC (111) interplanar distance is readily calculated from the nanoparticle number density.<sup>59</sup> Only one narrow wavelength spectral region will be diffracted by the FCC (111) planes for a specific incident angle of light on the PC (Figure 2). All wavelengths of light that do not meet the Bragg condition transmit through the PC except for a small

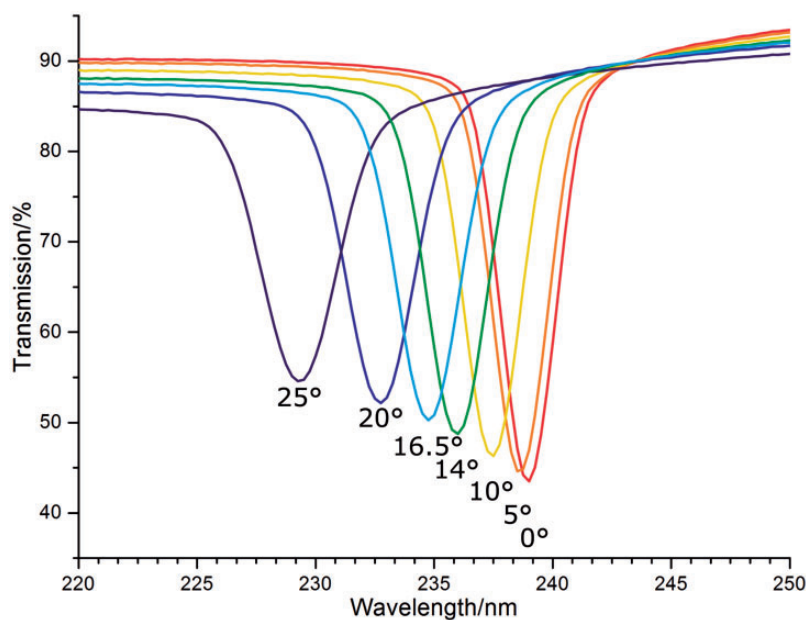


**Figure 2.**  $35.5 \pm 2.9$  nm silica nanoparticle PC transmission measured using an absorption spectrometer at various PC rotational angles.



**Figure 3.** Photograph of the PC cell. Highly charged, monodisperse nanoparticles are injected through the back plate into a cavity formed by a melted Parafilm spacer, where the particles self-assemble to form the deep UV diffracting PC.

amount of light that is diffusely scattered by the nanoparticles and a small amount of light that is reflected from the surfaces of the fused silica cell that encloses the PC.

The front face of the PC cell is wedge shaped (Thorlabs BSF2550) in order to direct unwanted reflected light out of the optical plane of the imaging spectrometer (Figure 3). The cell was constructed by utilizing a partially melted  $\sim 120 \mu\text{m}$  thick Parafilm spacer to attach the wedged

front face to a flat fused silica back plate. The highly charged nanoparticle dispersion was injected via a syringe through holes in the back plate. The nanoparticles immediately self-assemble to form the FCC PC where the (111) planes are oriented parallel to the cell surfaces.

Angle tuning the PC relative to the incident light tunes the wavelength of the diffracted narrow spectral region. We previously demonstrated that  $\sim 47$  nm diameter silica nanoparticles that diffract  $\sim 230$  nm light at normal incidence show  $\sim 5$  nm full width at half-maximum (FWHM) transmission bandwidths when measured using our absorption spectrometer.<sup>50</sup> The measured PC diffraction bandwidth is governed by the particle light scattering, particle ordering, light incident angle, and light collimation. The narrowest diffraction occurs for normal incident angles.<sup>34</sup> We reduced the normal incidence transmission bandwidth by  $\sim 46\%$  to  $\sim 2.7$  nm FWHM (Figure 2) measured in the absorption spectrometer by reducing the nanoparticle diameter from  $\sim 47$  nm in our previous work to  $35.5 \pm 2.9$  nm here. Reducing the diffraction bandwidth increases the spectral resolution of the Raman imaging spectrometer, enhancing the ability to differentiate between analytes with closely spaced Raman bands.

Smaller nanoparticle diameters and increased FCC ordering narrows the transmission and diffraction bandwidths.<sup>58,60,61</sup> Smaller nanoparticles and nanoparticles with refractive indices closer to that of the surrounding medium decrease the nanoparticle light scattering. For an optically thick PC, this allows a greater number of PC FCC planes to participate in diffraction, which narrows the diffraction spectral bandwidth.<sup>58,60</sup> Inhomogeneities in the nanoparticle spacings can derive from a lack of nanoparticle

size and charge monodispersity, or result from the formation of small polycrystalline domains due to imperfect self-assembly. This can result in a distribution of FCC (111) interplanar spacings that can broaden the diffraction bandwidth.<sup>58</sup> Determining the relative contribution of each of these phenomena is difficult since it requires complex studies of the dependence of diffraction bandwidth on all of the relevant PC material parameters.

The absorption spectrometer transmission measurements conveniently and quickly monitor the PC diffraction wavelengths and the transmission bandwidths for any incident angle. However, the PC diffraction bandwidths that determine the PC spectral imaging resolution are significantly narrower than the transmission bandwidths.<sup>61</sup> Furthermore, both the diffraction and transmission bandwidths are broadened for incident light that is imperfectly collimated, which results in a distribution of PC Bragg glancing angles. This phenomenon gives rise to an increased bandwidth for the transmission spectra measured by our absorption spectrometer which utilizes a noncollimated beam in the sample compartment.<sup>50</sup>

We directly measured the PC diffraction bandwidth by determining the angular dependence of the diffracted power of a 229 nm laser beam (Figure 4). Snell's Law was applied to the incident laser beam glancing angles measured in air to calculate the glancing angles within the PC, after refraction through the fused silica cell and into the PC (Figure 4a). A Gaussian fit depicted in blue (Figure 4a) was utilized to calculate the glancing angle for the maximum intensity of 229 nm diffraction ( $74.6^\circ$ ) and the angular FWHM bandwidth ( $\Delta\theta$ ,  $0.94^\circ$ ). The refractive index of the dispersion ( $n$ ) was calculated to be  $\sim 1.395$  using the volume fraction of nanoparticles (2.9%), the nanoparticle refractive index (assumed to be that of fused silica at 229 nm, 1.521), and the refractive index of water (1.391).<sup>62-64</sup> If we treat the PC diffraction in the more complete dynamical diffraction limit we will find a more complex relationship between the diffraction angle and the refractive index.<sup>61,65</sup> Given the calculated PC refractive index, we can use Bragg's Law in the kinematic limit to calculate the  $d_{111}$  plane spacing utilizing the measured glancing angle for the maximum intensity 229 nm diffraction (Eq. 2).

$$d_{hkl} = 229 \text{ nm} / 2 * 1.395 * \sin(74.6^\circ) = 85.2 \text{ nm} \quad (2)$$

We then utilized Bragg's Law to relate the angular bandwidth,  $\Delta\theta$ , to the wavelength bandwidth,  $\Delta\lambda$  (Eqs. 3 and 4). The limiting diffraction band glancing angles (FWHM,  $\theta_L$  and  $\theta_H$ ) are calculated by taking the difference between the center glancing angle and half of the angular FWHM ( $74.6 \pm 0.47^\circ$ ). The wavelength difference ( $\Delta\lambda$ ) between incident light at  $\theta_L$  and  $\theta_H$  (Eq. 4) yields the FWHM diffraction bandwidth in  $nm$ .

$$\lambda = 2 * 1.395 * 85.2 \text{ nm} * \sin(\theta) = 238 * \sin(\theta) \quad (3)$$

$$\begin{aligned} \Delta\lambda &= |[238\sin(\theta_L)] - [238\sin(\theta_H)]| \\ &= |[238\sin(74.1)] - [238\sin(75.1)]| = 1.0 \text{ nm} \end{aligned} \quad (4)$$

We measured a maximum diffraction efficiency of  $\sim 50\%$  at a glancing angle of  $74.4^\circ$  (Figure 4a). We measured a bandwidth of  $\sim 4.0$  nm FWHM for PC transmission at a glancing angle of  $74^\circ$  in our absorption spectrometer (Figure 4b), which is approximately four times larger than the calculated bandwidth measured via the laser beam intensity diffraction method (Figure 4a).

During the 229 nm laser beam intensity measurements, we discovered that extended 229 nm laser beam irradiation causes local PC disorder likely due to photochemical reactions that presumably increase ionic strength. The beam intensity used was too small to give rise to photothermal effects due to local heating.<sup>66,67</sup> These PC photochemical reactions will be negligible during UV Raman imaging due to the weak incident UV power produced by UV Raman photons.

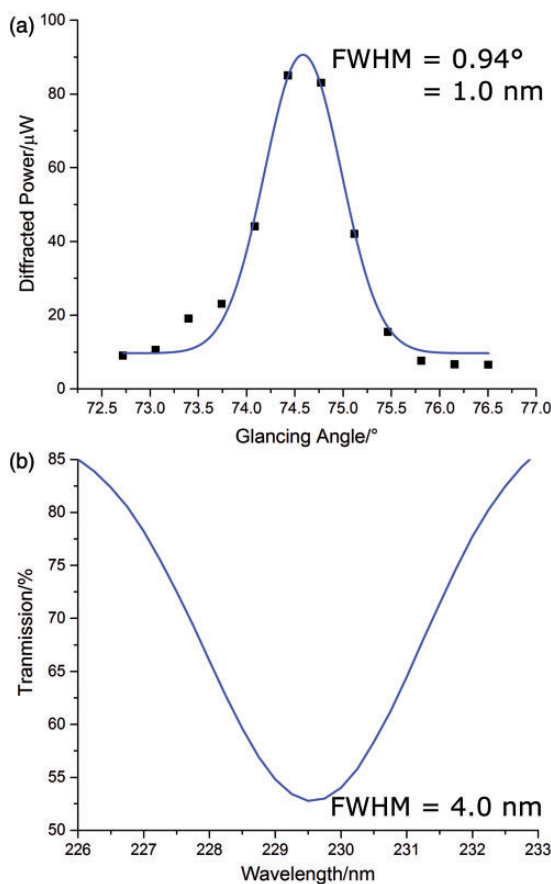
### UV Wide-Field Imaging Spectrometer Design

Figure 5 shows a schematic of our deep UV wide-field imaging spectrometer. We utilized a custom-built Maksutov-Cassegrain telescope (Questar 3.5 in. Field Model) optimized for deep UV transmission to collect Raman scattered light from a 2.3 m standoff distance. A 229/244 nm dual notch filter (NF, Semrock NF01-229/244-25) was attached to the exit port of the telescope to reject Rayleigh scattered light. The collected light was collimated using a 2 in. diameter plano-convex lens (L1).

The PC diffraction angle was set by a computer-controlled rotational stage (Zaber X-RSW60A, fine resolution, low speed model) to enable precise, reproducible tuning of the PC angle. Prior to Raman imaging, a  $1280 \times 1024$  color CMOS camera (CMOS, Thorlabs DCC1645C) with a 35 mm f/2.0 lens (Thor Labs MVL35M23) was used to image the sample using ambient visible light. This image also enabled alignment of the spectrometer with respect to the sample.

The Raman light diffracted by the PC was directed to a 2" diameter planar UV enhanced mirror (M, CVI Laser Optics DUVA-PM-2037-UV) mounted to a rotational (Zaber X-RSW60A) and translational stage (Zaber T-LSM200A, 200 mm travel). Mirror M directed the diffracted Raman scattered light through the center of lens L2. A 2 in. plano-convex lens (L2) mounted to a translational stage (Zaber T-LSM050A, 50 mm travel) focused the Raman image onto the CCD.

A solar blind UV bandpass filter (UBF, Acton Optics FB240-B-2D) was mounted directly to the face of the CCD detector to reduce interference from ambient light and sample luminescence. The UBF has a peak transmission



**Figure 4.** (a) Diffraction power of the 229 nm laser beam diffracted by PC in panel (b) as a function of laser glancing angle within the PC dispersion. Incident beam power is  $\sim 150 \mu\text{W}$ . A Gaussian fit is depicted in blue. (b) PC transmission measured in the absorption spectrometer at a  $68^\circ$  glancing angle measured in air ( $74^\circ$  within PC after refraction).

of 40% at 237 nm, a FWHM of 32 nm, and  $>2.5$  OD in the range of 350–1100 nm. A thermoelectrically cooled CCD detector (CCD, Princeton Instruments PIXIS 1024 BU,  $1024 \times 1024$ ,  $13 \times 13 \mu\text{m}$  pixels) was utilized to collect deep UV Raman images. The Raman image S/N was increased by sacrificing image resolution through hardware binning of adjacent CCD pixels into super-pixels prior to image readout. Pixel binning of  $8 \times 8$  and  $6 \times 6$  was utilized for the 30 s and 2 min image accumulation times, respectively.

The imaging spectrometer was constructed inside a light-tight optical enclosure utilizing construction rails and black hardboard (Thorlabs). The spectrometer was mounted to a  $4 \times 2'$  breadboard (Melles Griot) attached to a wheeled cart (Thorlabs Optics a la Cart).

### Raman Wide-Field Imaging

We utilized this deep UV wide-field imaging spectrometer to detect explosive films of AN and PETN. The drop-cast explosive samples (Figure 6), and the inkjet printed

explosive samples (Figures 7 and 8), were placed 2.3 m in front of the imaging spectrometer telescope. The samples were centered along the spectrometer's optical axis by using the imaging spectrometer CMOS camera. We then directed the  $\sim 1.2 \times 1.2$  cm expanded 229 nm beam to excite the explosive samples. The telescope collected the Raman scattered light, which was collimated and directed onto the PC. Prior to imaging, the PC was angle tuned to diffract a spectral region centered on the most intense Raman bands of each explosive.

A  $16.5^\circ$  PC rotational angle was utilized to diffract the spectral region centered about the intense  $\text{AN } 1044 \text{ cm}^{-1} \text{ NO}_3^-$  symmetric stretching band (Figure 6b). At this PC angle, the AN film shows a much larger Raman image intensity than the PETN film (Figure 6c and d) due to the large Raman solid state cross-section of the  $1044 \text{ cm}^{-1}$  AN band, previously measured by Emmons et al. to be  $3.4 \times 10^{-26} \text{ cm}^2/\text{mol}\cdot\text{sr}$ .<sup>49</sup> The PETN film surprisingly shows a weak but significant Raman image intensity despite a lack of a PETN Raman band within the PC band FWHM diffraction spectral region. We expect small intensity contributions from the adjacent  $1269$  and  $1289 \text{ cm}^{-1}$  Raman bands because they will be diffracted by the PC diffraction tails (Figure 4a). We also expect a small broadening of the PC diffraction bandwidth due to imperfections in the collimation of Raman light within the imaging spectrometer. In addition, there may also be contributions to the PETN image intensity due to the formation of PETN photoproducts. We recently discovered that PETN photolysis in the presence of water will produce  $\text{NO}_3^-$  which will give rise to PETN image intensity resulting from the  $\text{NO}_3^-$  symmetric stretching band.\*

The image intensity ( $I_R$ ) of each pure analyte film should scale with the Raman cross-sections ( $\sigma$ ) of the Raman bands diffracted by the PC and the number of molecules ( $N$ ) involved in the Raman scattering (Eq. 5).

$$I_R \sim \sigma * N \quad (5)$$

The number of analyte molecules involved in this Raman scattering depends upon the attenuation of the incident beam within the film due to absorption as well as due to elastic light scattering due to refractive index inhomogeneities (Eq. 6).<sup>68</sup>

$$I_R \sim \sigma * \rho / m(\epsilon + \gamma) \quad (6)$$

Where  $\rho$  is the film density,  $m$  is the analyte molecular weight,  $\epsilon$  is the molar absorptivity of the analyte at 229 nm, and  $\gamma$  is the effective attenuation factor due to elastic light scattering.

\*K.L. Gares, S.V. Bykov, B. Godugu, and S.A. Asher, "UV Resonance Raman Pentaerythritol Tetranitrate (PETN) Solution Photochemistry". Unpublished Manuscript. 2016.

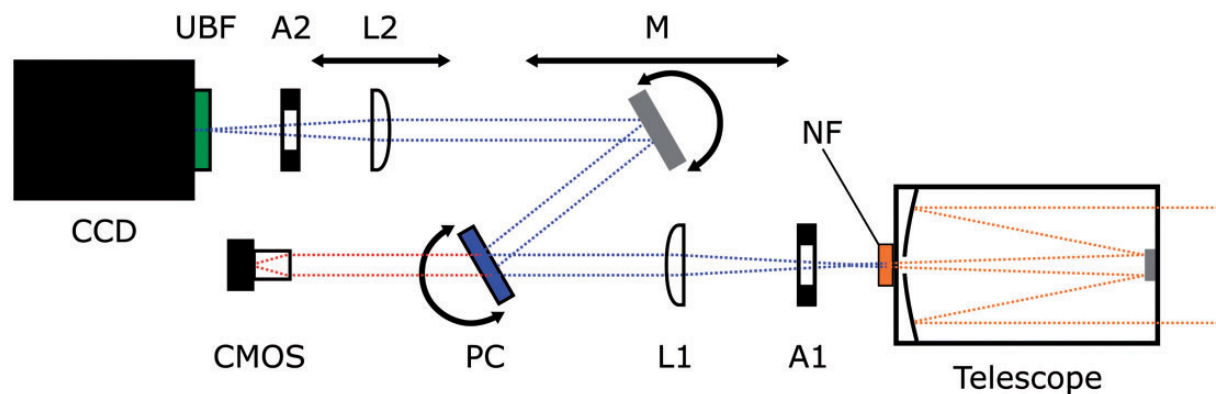


**Figure 5.** Schematic of the standoff deep UV hyperspectral Raman imaging spectrometer. NF, 229 nm notch filter; A1, aperture; L1, plano-convex collimating lens; PC, UV diffracting photonic crystal mounted on a rotational stage, CMOS, color camera with 35 mm lens; M, planar mirror mounted on a rotational stage connected to a translational stage; L2, plano-convex focusing lens mounted on a translational stage; A2, aperture; UBF, UV bandpass filter; CCD, PIXIS detector.  $f_{L1} = 205$  mm and  $f_{L2} = 95$  mm at 229 nm.

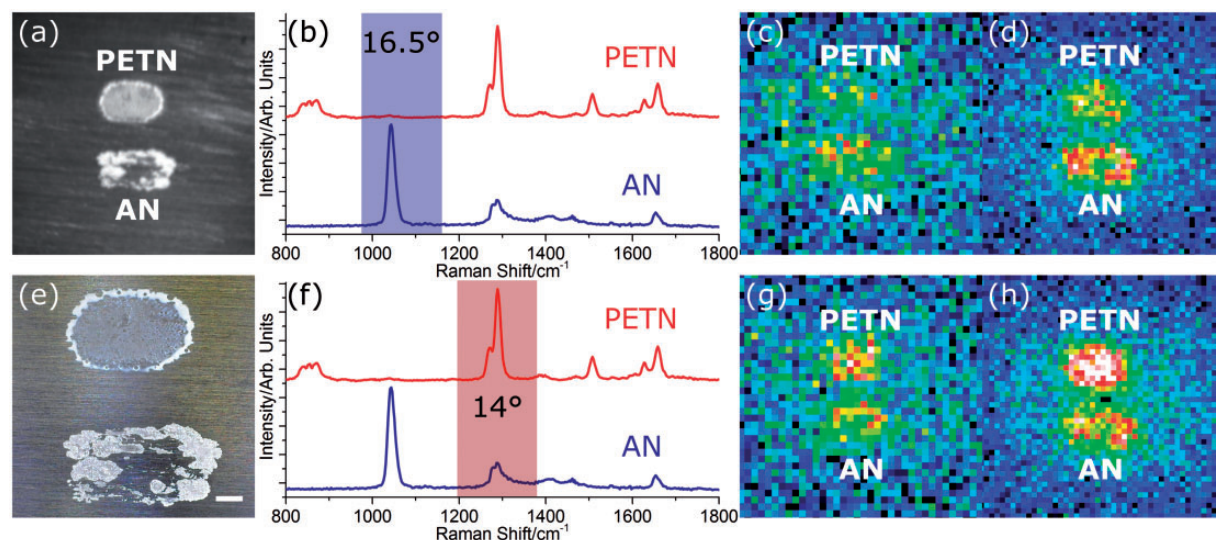


**Figure 6.** (a) CMOS image of the  $120 \mu\text{g}$  ( $920 \mu\text{g}/\text{cm}^2$ ) PETN (top) and  $120 \mu\text{g}$  ( $760 \mu\text{g}/\text{cm}^2$ ) AN (bottom) drop-cast films on an aluminum plate at a 2.3 m standoff distance. (b) 229 nm Raman spectra of solid PETN (top, red) and solid AN (bottom, blue). A  $\sim 1$  nm FWHM diffracted spectral bandwidth at a  $16.5^\circ$  PC angle is depicted by the blue shading. (c, d) Raman images of the trace explosive sample shown in (a) at a  $16.5^\circ$  PC angle after 30 s and 2 min accumulations, respectively. (e) Expanded  $30\times$  microscope image of the sample in panel (a) before irradiation. Scale bar represents 1 mm. (f) 229 nm Raman spectra of solid PETN (top) and solid AN (bottom). A  $\sim 1$  nm FWHM diffracted spectral bandwidth at a  $14^\circ$  PC angle is depicted by the red shading. (g, h) Raman images of the trace explosives shown in (a) at a  $14^\circ$  PC angle after 30 s and 2 min accumulations, respectively. Both rotational angles of incidence are measured in air. Thirty second and 2 min accumulations utilize  $8 \times 8$  and  $6 \times 6$  pixel binning, respectively.

The image intensity may also depend upon film thickness. In the thick film limit where the beam is completely attenuated as it traverses the film, the number of Raman scattering molecules depends on the penetration depth of the beam through the film. The beam penetration depth is inversely proportional to the molar absorptivity of the sample and to elastic scattering due to refractive index inhomogeneities  $(\epsilon + \gamma)^{-1}$ . In the thick film limit,

the Raman intensity is independent of film thickness. In contrast, in the thin film limit the exciting beam is not completely attenuated before traversing the entire film thickness. In this case, the Raman image intensity is proportional to film thickness. The AN drop-cast sample is partially in the thin film limit since the exterior of the AN film shows higher Raman image intensity than the thinner center of the film (Figure 6d). Crystallite orientation within

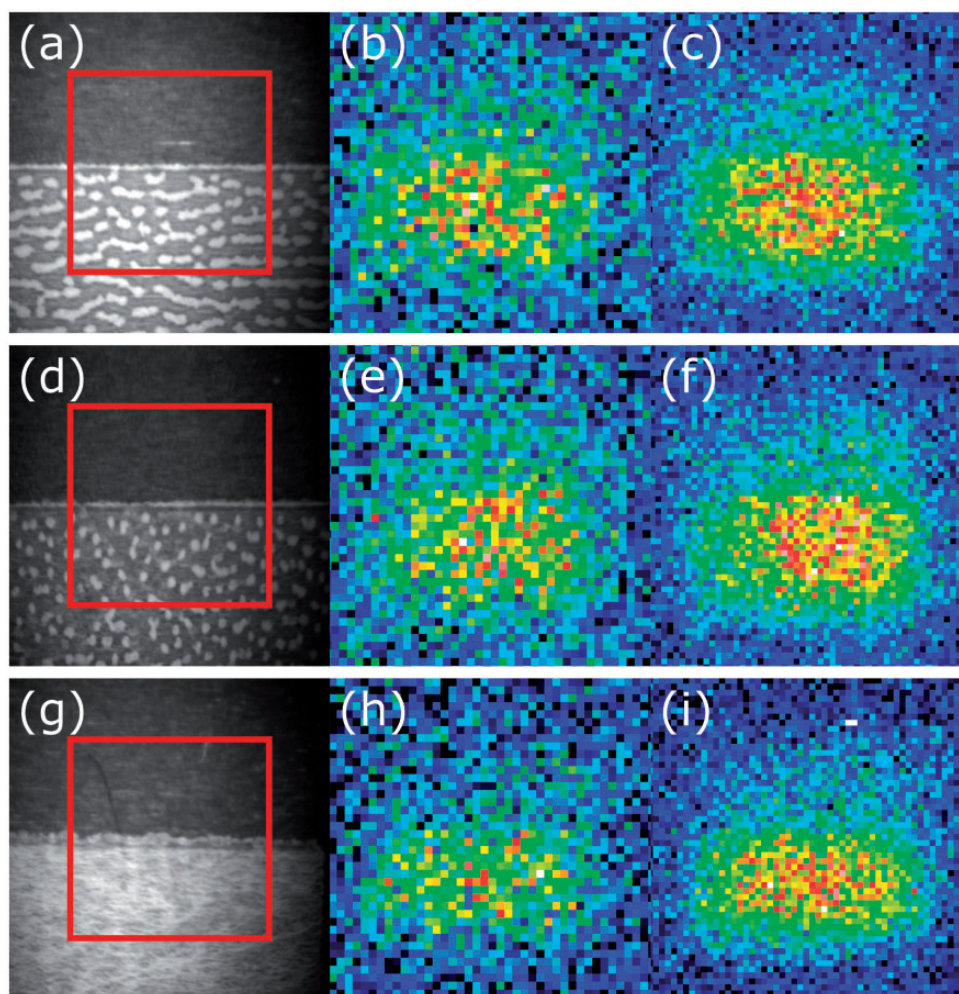


**Figure 7.** (a, d, g) CMOS images of  $250 \mu\text{g}/\text{cm}^2$ ,  $100 \mu\text{g}/\text{cm}^2$ , and  $10 \mu\text{g}/\text{cm}^2$  inkjet printed PETN on smooth aluminum substrates, respectively, at a 2.3 m standoff distance. Red outlines indicate the area illuminated with 229 nm excitation. (b, e, h) Raman images of the trace explosives shown in panels (a, d, g) at a  $13^\circ$  PC angle at 30 s ( $8 \times 8$  binning) of accumulation. (c, f, i) Raman images of the trace explosives shown in panels (a, d, g), at a PC angle of  $13^\circ$  at 2 min ( $6 \times 6$  binning) of accumulation. The PC used here differs from that used in Figure 6. At a  $13^\circ$  PC angle, the PC diffracts a Raman spectral region centered at the  $1289 \text{ cm}^{-1}$  PETN  $\text{NO}_2$  symmetric stretch.

the films could also affect Raman image intensities. We are presently investigating the influence of film morphology on Raman image intensity.

In contrast, a  $14^\circ$  PC rotational angle was utilized to diffract the Raman spectral region centered about the intense PETN  $1289 \text{ cm}^{-1}$   $\text{NO}_2$  symmetric stretching band (Figure 6f).<sup>1,69,70</sup> Emmons et al. measured an  $3.2 \times 10^{-26} \text{ cm}^2/\text{molc}\cdot\text{str}$  effective solid state Raman cross-section sum for the PETN  $1289 \text{ cm}^{-1}$  band and the overlapping shoulder at  $1269 \text{ cm}^{-1}$ .<sup>49</sup> For solid AN, this region contains the  $\text{NO}_3^-$  anti-symmetric stretching Raman band at  $\sim 1288 \text{ cm}^{-1}$ .<sup>49,71,72</sup> We estimate a solid state Raman cross-section of  $1.7 \times 10^{-26} \text{ cm}^2/\text{molc}\cdot\text{str}$  for the AN  $1288 \text{ cm}^{-1}$  anti-symmetric stretching band. Thus, at the  $14^\circ$  PC angle the image intensity of PETN band should exceed that of AN (Figure 6g and h).

We also measured deep UV Raman images of  $250 \mu\text{g}/\text{cm}^2$ ,  $100 \mu\text{g}/\text{cm}^2$ , and  $10 \mu\text{g}/\text{cm}^2$  PETN and AN films deposited on smooth aluminum substrates via inkjet printing (Figures 7 and 8). The sample surfaces illuminated by the 229 nm laser include a lower region covered with an explosive as well as an upper, expectedly bare, aluminum region. It should be noted that a different PC with different diffraction angles was utilized for imaging these inkjet printed explosive samples. High S/N Raman images were collected for all PETN inkjet samples with short accumulation times and low surface coverages (Figure 7). Pentaerythritol tetranitrate is easily detectable at  $10 \mu\text{g}/\text{cm}^2$  due to the uniform surface coverage. The mounds of PETN visible in the CMOS images of the  $250$  and  $100 \mu\text{g}/\text{cm}^2$  inkjet samples (Figure 7a and d) are not visible in the UV Raman images (Figure 7b, c, e, and f) because of the

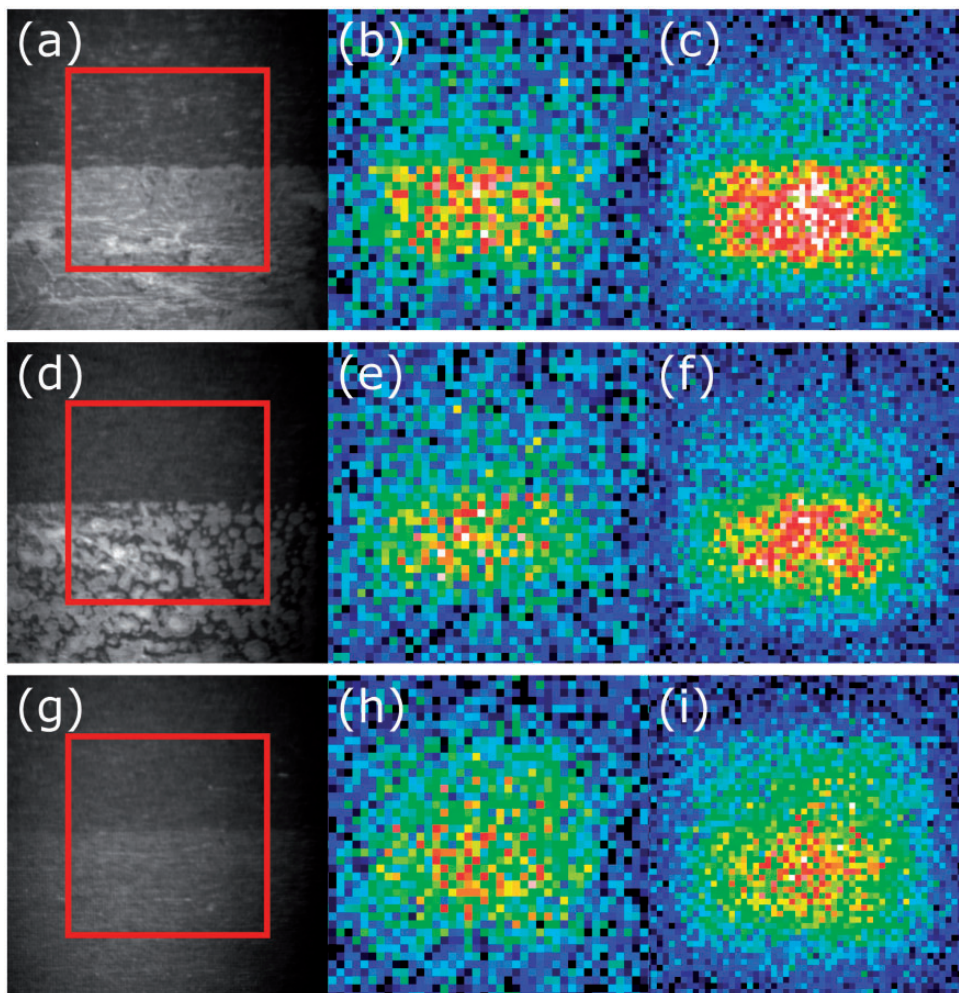


**Figure 8.** (a, d, g) CMOS images of  $250 \mu\text{g}/\text{cm}^2$ ,  $100 \mu\text{g}/\text{cm}^2$ , and  $10 \mu\text{g}/\text{cm}^2$  inkjet printed AN on smooth aluminum substrates, respectively, at a 2.3 m standoff distance. Red outlines indicate the areas illuminated with 229 nm excitation. (b, e, h) Raman images of the trace explosives shown in panels (a, d, g), at a  $16^\circ$  PC angle at 30 s ( $8 \times 8$  binning) of accumulation. (c, f, i) Raman images of the trace explosives shown in panels (a, d, g), at a  $16^\circ$  PC angle at 2 min ( $6 \times 6$  binning) accumulations. At a  $16^\circ$  PC angle, the PC diffracts a Raman spectral region centered at the  $1044 \text{ cm}^{-1}$  AN  $\text{NO}_3^-$  symmetric stretch. The diffracting PC used here is identical to that used in Figure 7.

presence of optically thick PETN in the regions between the mounds. Since PETN is present between the large visible mounds, we expect that the uninterrupted optically thick PETN film should produce roughly uniform Raman image intensity.

The similar Raman image intensities observed for all three PETN inkjet samples (Figure 7c, f, and i) also indicate that these samples are all optically thick. The observed Raman image intensity will decrease only when the PETN films become sufficiently thin such that the incident 229 nm laser beam is no longer fully attenuated before traversing the entire thickness of the film. Given the high S/N images collected at a surface coverage of  $10 \mu\text{g}/\text{cm}^2$ , we estimate a detection limit of  $\sim 1 \mu\text{g}/\text{cm}^2$  for PETN under these experimental conditions and for films uniformly distributed across the substrate surface.

$\text{NH}_4\text{NO}_3$  is also easily detectable in high S/N Raman images for the  $250$  and  $100 \mu\text{g}/\text{cm}^2$  samples (Figure 8). However, for the  $10 \mu\text{g}/\text{cm}^2$  AN sample, it becomes challenging to differentiate the edge between deposited AN and the adjacent aluminum surface (Figure 8h and i). During these measurements, we observed that high lab humidity quickly led to deliquescence (Figure 8d and g) of hygroscopic AN samples. We hypothesize that vaporization and re-deposition<sup>73</sup> or efflorescence-like migration<sup>74,75</sup> of AN may decrease the sharpness of the AN film/aluminum interface.

In contrast to the PETN inkjet samples, the AN Raman image intensity decreases with decreasing amounts of deposited AN (Figure 8c, f, and i). As the amount of deposited AN decreases, the film becomes less homogeneous and optically thin areas become evident in both the

microscope and color CMOS images (Figure 8d and g), resulting in less Raman image intensity. We also estimate a detection limit of  $\sim 1 \mu\text{g}/\text{cm}^2$  for AN under these experimental conditions and for films uniformly distributed across the substrate surface.

## Conclusion

We demonstrated that our novel deep UV diffracting PCs enable the construction of the first wide-field UV imaging spectrometer for the standoff detection of trace explosives. We utilized our UV Raman wide-field imaging spectrometer to detect and image 10–1000  $\mu\text{g}/\text{cm}^2$  PETN and AN films on aluminum substrates at 2.3 m standoff distances with 229 nm excitation. We observed UV Raman images of sample surfaces that depict the deposition morphologies of these explosives and allow them to be chemically differentiated. We estimate a detection limit of  $\sim 1 \mu\text{g}/\text{cm}^2$  for PETN and AN under these experimental conditions for films uniformly distributed across the substrate surface. The  $\sim 1$  nm PC diffraction bandwidth demonstrated here is still relatively broad. We are presently optimizing our PCs to narrow the bandwidth of the diffracted spectral region in order to increase the spectral resolution of our UV imaging spectrometer. Increasing the PC nanoparticle size monodispersity and charge will improve the ordering of the PC, narrowing the diffracted spectral bandwidths. We are currently working to optimize and miniaturize our UV imaging spectrometer by improving our PC technology and miniaturizing our novel deep UV laser sources.

## Acknowledgments

The authors thank the Pitt Chemistry Machine Shop for machining sample substrates and spectrometer adapter pieces as well as the US Army Research Lab for generously donating inkjet printed explosive samples.

## Conflict of Interest

The authors report there are no conflicts of interest.

## Funding

The authors received funding from the Office of Naval Research (ONR) N00014-12-1-0021 and N00014-16-1-2681 grants and the Department of Defense/Technology Commercialization Consortium/Innovation Works (DOD/TCC/IW) grant, DOD award number OEA ST 1429.14.01, Commonwealth of Pennsylvania contract number C000061864.

## References

1. K.L. Gares, K.T. Hufziger, S.V. Bykov, S.A. Asher. "Review of Explosive Detection Methodologies and the Emergence of Standoff Deep UV Resonance Raman". *J. Raman Spectrosc.* 2016. 47(1): 124–141.
2. M. Marshall, J.C. Oxley. *Aspects of Explosives Detection*. Oxford: Elsevier, 2009.
3. E.D. Emmons, A. Tripathi, J.A. Guicheteau, S.D. Christesen, A.W. Fountain. "Raman Chemical Imaging of Explosive-Contaminated Fingerprints". *Appl. Spectrosc.* 2009. 63(11): 1197–1203.
4. P. Lucena, I. Gaona, J. Moros, J.J. Laserna. "Location and Detection of Explosive-Contaminated Human Fingerprints on Distant Targets Using Standoff Laser-Induced Breakdown Spectroscopy". *Spectrochim. Acta B.* 2013. 85: 71–77.
5. C. Lopez-Moreno, S. Palanco, J.J. Laserna, F.C. De Lucia, A.W. Miziolek, J. Rose, R.A. Walters, A.I. Whitehouse. "Test of a Stand-Off Laser-Induced Breakdown Spectroscopy Sensor for the Detection of Explosive Residues on Solid Surfaces". *J. Anal. At. Spectrom.* 2006. 21(1): 55–60.
6. C.J. Cumming, C. Aker, M. Fisher, M. Fok, M.J. La Grone, D. Reust, M.G. Rockley, T.M. Swager, E. Towers, V. Williams. "Using Novel Fluorescent Polymers as Sensory Materials for Above-Ground Sensing of Chemical Signature Compounds Emanating from Buried Landmines". *IEEE T. Geosci. Remote.* 2001. 39(6): 1119–1128.
7. H. Ostmark, S. Wallin, H.G. Ang. "Vapor Pressure of Explosives: A Critical Review". *Propell. Explos. Pyrot.* 2012. 37(1): 12–23.
8. A.W. Fountain, S.D. Christesen, R.P. Moon, J.A. Guicheteau, E.D. Emmons. "Recent Advances and Remaining Challenges for the Spectroscopic Detection of Explosive Threats". *Appl. Spectrosc.* 2014. 68(8): 795–811.
9. T.L. Andrew, T.M. Swager. "Detection of Explosives via Photolytic Cleavage of Nitroesters and Nitramines". *J. Org. Chem.* 2011. 76(9): 2976–2993.
10. R.R. Kunz, K.E. Gregory, M.J. Aernecke, M.L. Clark, A. Ostrinskaya, A.W. Fountain. "Fate Dynamics of Environmentally Exposed Explosive Traces". *J. Phys. Chem. A.* 2012. 116(14): 3611–3624.
11. K.L. Gares, S.V. Bykov, T. Brinzer, S.A. Asher. "Solution and Solid Hexahydro-1, 3, 5-trinitro-1, 3, 5-triazine (RDX) Ultraviolet (UV) 229 nm Photochemistry". *Appl. Spectrosc.* 2015. 69(5): 545–554.
12. K.L. Gares, S.V. Bykov, B. Godugu, S.A. Asher. "Solution and Solid Trinitrotoluene (TNT) Photochemistry: Persistence of TNT-like Ultraviolet (UV) Resonance Raman Bands". *Appl. Spectrosc.* 2013. 68(1): 49–56.
13. M. Ghosh, L. Wang, S.A. Asher. "Deep-Ultraviolet Resonance Raman Excitation Profiles of  $\text{NH}_4\text{NO}_3$ , PETN, TNT, HMX, and RDX". *Appl. Spectrosc.* 2012. 66(9): 1013–1021.
14. D.D. Tuschel, A.V. Mikhonin, B.E. Lemoff, S.A. Asher. "Deep Ultraviolet Resonance Raman Excitation Enables Explosives Detection". *Appl. Spectrosc.* 2010. 64(4): 425–432.
15. S.V. Bykov, M. Mao, K.L. Gares, S.A. Asher. "Compact Solid-State 213 nm Laser Enables Standoff Deep Ultraviolet Raman Spectrometer: Measurements of Nitrate Photochemistry". *Appl. Spectrosc.* 2015. 69(8): 895–901.
16. R.J. Harper, K.G. Furton. "Biological Detection of Explosives". In: J. Yinon (ed.) *Counterterrorist Detection Techniques of Explosives*. Oxford: Elsevier, 2007, pp.395–432.
17. G.A. Eiceman, Z. Karpas, H.H. Hill Jr. "Detection of Explosives by IMS". *Ion Mobility Spectrometry*. Boca Raton, FL: CRC Press, 2013, pp.269–287.
18. M.E. Germain, M.J. Knapp. "Optical Explosives Detection: From Color Changes to Fluorescence Turn-On". *Chem. Soc. Rev.* 2009. 38(9): 2543–2555.
19. S.A. Oladepo, K. Xiong, Z. Hong, S.A. Asher, J. Handen, I.K. Lednev. "UV Resonance Raman Investigations of Peptide and Protein Structure and Dynamics". *Chem. Rev.* 2012. 112(5): 2604–2628.
20. S.A. Asher. "Ultraviolet Raman Spectrometry". In: J.M. Chalmers, P.R. Griffiths (eds) *Handbook of Vibrational Spectroscopy*. Hoboken, NJ: John Wiley & Sons, 2002, pp.1–15.
21. S.A. Asher. "UV Resonance Raman Spectroscopy for Analytical, Physical, and Biophysical Chemistry". *Anal. Chem.* 1993. 65(4): 201A–210A.

22. J.C. Carter, S.M. Angel, M. Lawrence-Snyder, J. Scaffidi, R.E. Whipple, J.G. Reynolds. "Standoff Detection of High Explosive Materials at 50 Meters in Ambient Light Conditions Using a Small Raman Instrument". *Appl. Spectrosc.* 2005. 59(6): 769–775.
23. A.K. Misra, S.K. Sharma, T.E. Acosta, J.N. Porter, D.E. Bates. "Single-Pulse Standoff Raman Detection of Chemicals from 120 m Distance During Daytime". *Appl. Spectrosc.* 2012. 66(11): 1279–1285.
24. M. Nelson, P. Treado. "Raman Imaging Instrumentation". In: S. Sasic, Y. Ozaki (eds) *Raman, Infrared, and Near-infrared Chemical Imaging*. Hoboken, NJ: John Wiley & Sons, 2011, pp.23–51.
25. G. Steiner. "Infrared and Raman Spectroscopic Imaging". In: R. Salzer (ed.) *Biomedical Imaging: Principles and Applications*. Hoboken, NJ: John Wiley & Sons, 2010, pp.275–303.
26. S. Schlücker, M.D. Schaeberle, S.W. Huffman, I.W. Levin. "Raman Microspectroscopy: A Comparison of Point, Line, and Wide-Field Imaging Methodologies". *Anal. Chem.* 2003. 75(16): 4312–4318.
27. Y. Kumamoto, A. Taguchi, N.I. Smith, S. Kawata. "Deep Ultraviolet Resonant Raman Imaging of a Cell". *J. Biomed. Opt.* 2012. 17(7): 0760011–0760014.
28. G. Puppels, M. Grond, J. Greve. "Direct Imaging Raman Microscope Based on Tunable Wavelength Excitation and Narrow-Band Emission Detection". *Appl. Spectrosc.* 1993. 47(8): 1256–1267.
29. K.T. Hufziger, S.V. Bykov, S.A. Asher. "Raman Hyperspectral Imaging Spectrometer Utilizing Crystalline Colloidal Array Photonic Crystal Diffraction". *Appl. Spectrosc.* 2014. 68(11): 1219–1223.
30. H. Östmark, M. Nordberg, T.E. Carlsson. "Stand-Off Detection of Explosives Particles by Multispectral Imaging Raman Spectroscopy". *Appl. Opt.* 2011. 50(28): 5592–5599.
31. S.A. Asher. Crystalline colloidal narrow band radiation filter. US4632517. Filed 1984. Issued 1986.
32. S.A. Asher. Crystalline colloidal narrow band radiation filter. US4627689. Filed 1983. Issued 1986.
33. S.A. Asher, P. Flaugh. "Crystalline Colloidal Bragg Diffraction Devices: The Basis for a New Generation of Raman Instrumentation". *Spectroscopy*. 1986. 1(12): 26–31.
34. P. Flaugh, S. O'Donnell, S.A. Asher. "Development of a New Optical Wavelength Rejection Filter: Demonstration of Its Utility in Raman Spectroscopy". *Appl. Spectrosc.* 1984. 38(6): 847–850.
35. S.A. Asher, J. Holtz, L. Liu, Z. Wu. "Self-Assembly Motif for Creating Submicron Periodic Materials. Polymerized Crystalline Colloidal Arrays". *J. Am. Chem. Soc.* 1994. 116(11): 4997–4998.
36. M. Ben-Moshe, V.L. Alexeev, S.A. Asher. "Fast Responsive Crystalline Colloidal Array Photonic Crystal Glucose Sensors". *Anal. Chem.* 2006. 78(14): 5149–5157.
37. J.-T. Zhang, Z. Cai, D.H. Kwak, X. Liu, S.A. Asher. "Two-Dimensional Photonic Crystal Sensors for Visual Detection of Lectin Concanavalin A". *Anal. Chem.* 2014. 86(18): 9036–9041.
38. Z. Cai, D.H. Kwak, D. Punihaoale, Z. Hong, S.S. Velankar, X. Liu, S.A. Asher. "A Photonic Crystal Protein Hydrogel Sensor for *Candida Albicans*". *Angew. Chem. Int. Ed.* 2015. 54(44): 13036–13040.
39. H.R. Morris, C.C. Hoyt, P.J. Treado. "Imaging Spectrometers for Fluorescence and Raman Microscopy: Acousto-Optic and Liquid Crystal Tunable Filters". *Appl. Spectrosc.* 1994. 48(7): 857–866.
40. A. Pettersson, I. Johansson, S. Wallin, M. Nordberg, H. Östmark. "Near Real-Time Standoff Detection of Explosives in a Realistic Outdoor Environment at 55 m Distance". *Propell. Explos. Pyrot.* 2009. 34(4): 297–306.
41. B. Zachhuber, G. Ramer, A. Hobro, B. Lendl. "Stand-off Raman Spectroscopy: A Powerful Technique for Qualitative and Quantitative Analysis of Inorganic and Organic Compounds Including Explosives". *Anal. Bioanal. Chem.* 2011. 400(8): 2439–2447.
42. A. Ehlerding, I. Johansson, S. Wallin, H. Östmark. "Resonance-Enhanced Raman Spectroscopy on Explosives Vapor at Standoff Distances". *Int. J. Spectrosc.* 2012. 2012): 1–9.
43. R. Bhartia, W.F. Hug, R.D. Reid. "Improved Sensing Using Simultaneous Deep UV Raman and Fluorescence Detection". *Proc. SPIE 8358, Chemical, Biological, Radiological, Nuclear, and Explosives (CBRNE) Sensing XIII*. 2012. 8358: p. 83581 A.
44. A.J. Hopkins, J.L. Cooper, L.T.M. Profeta, A.R. Ford. "Portable Deep-Ultraviolet (DUV) Raman for Standoff Detection". *Appl. Spectrosc.* 2016. 70(5): 861–873.
45. S.A. Asher. "UV Resonance Raman Spectroscopy for Analytical, Physical, and Biophysical Chemistry". *Anal. Chem.* 1993. 65(2): 59 A–66 A.
46. S.A. Asher, C. Johnson. "Raman Spectroscopy of a Coal Liquid Shows that Fluorescence Interference Is Minimized with Ultraviolet Excitation". *Science*. 1984. 225(4659): 311.
47. American National Standards Institute. American National Standard for Safe Use of Lasers, ANSI Z136.1. Orlando, FL: Laser Institute of America, 2014.
48. J.A. Carroll, E.L. Izake, B. Cletus, E. Jaatinen. "Eye-Safe UV Stand-Off Raman spectroscopy for the Ranged Detection of Explosives in the Field". *J. Raman Spectrosc.* 2015. 46(3): 333–338.
49. E.D. Emmons, A. Tripathi, J.A. Guicheteau, A.W. Fountain III, S.D. Christesen. "Ultraviolet Resonance Raman Spectroscopy of Explosives in Solution and the Solid State". *J. Phys. Chem. A*. 2013. 117(20): 4158–4166.
50. L. Wang, A. Tikhonov, S.A. Asher. "Silica Crystalline Colloidal Array Deep Ultraviolet Narrow-Band Diffraction Devices". *Appl. Spectrosc.* 2012. 66(4): 426–431.
51. K.D. Hartlen, A.P.T. Athanopoulos, V. Kitaev. "Facile Preparation of Highly Monodisperse Small Silica Spheres (15 to >200 nm) Suitable for Colloidal Templating and Formation of Ordered Arrays". *Langmuir*. 2008. 24(5): 1714–1720.
52. NIH. ImageJ. <https://imagej.nih.gov/ij/index.html> [accessed August 2016].
53. S.A. Asher, R.W. Borrett, X. Chen, D.H. Lemmon, N. Cho, P. Peterson, M. Arrigoni, L. Spinelli, J. Cannon. "UV Resonance Raman Spectroscopy Using a New CW Laser Source: Convenience and Experimental Simplicity". *Appl. Spectrosc.* 1993. 47(5): 628–633.
54. R.D. Deegan, O. Bakajin, T.F. Dupont, G. Huber, S.R. Nagel, T.A. Witten. "Contact Line Deposits in an Evaporating Drop". *Phys. Rev. E*. 2000. 62(1): 756.
55. G. Gillen and J.R. Verkouteren. "Standards for standoff optical-based explosives detection", In: K. Iniewski (ed) *Laser-Based Optical Detection of Explosives*. Boca Raton: Taylor & Francis, 2015. pp. 41–63.
56. E.L. Holthoff, M.E. Farrell, P.M. Pellegrino. "Standardized Sample Preparation Using a Drop-On-Demand Printing Platform". *Sensors*. 2013. 13(5): 5814–5825.
57. S.A. Asher, C.R. Johnson, J. Murtaugh. "Development of a New UV Resonance Raman Spectrometer for the 217–400-nm Spectral Region". *Rev. Sci. Instrum.* 1983. 54(12): 1657–1662.
58. S.A. Asher, J.M. Weissman, A. Tikhonov, R.D. Coalson, R. Kesavamoorthy. "Diffraction in Crystalline Colloidal-Array Photonic Crystals". *Phys. Rev. E*. 2004. 69(6): 066619.
59. R.J. Carlson, S.A. Asher. "Characterization of Optical Diffraction and Crystal Structure in Monodisperse Polystyrene Colloids". *Appl. Spectrosc.* 1984. 38(3): 297–304.
60. R.J. Spry, D.J. Kosan. "Theoretical Analysis of the Crystalline Colloidal Array Filter". *Appl. Spectrosc.* 1986. 40(6): 782–784.
61. P.A. Rundquist, P. Photinos, S. Jagannathan, S.A. Asher. "Dynamical Bragg Diffraction from Crystalline Colloidal Arrays". *J. Chem. Phys.* 1989. 91(8): 4932–4941.
62. I.H. Malitson. "Interspecimen Comparison of the Refractive Index of Fused Silica". *J. Opt. Soc. Am.* 1965. 55(10): 1205–1209.
63. M. Daimon, A. Masumura. "Measurement of the Refractive Index of Distilled Water from the Near-Infrared Region to the Ultraviolet Region". *Appl. Opt.* 2007. 46(18): 3811–3820.

64. G. Pan, A.K. Sood, S.A. Asher. "Polarization Dependence of Crystalline Colloidal Array Diffraction". *J. Appl. Phys.* 1998. 84(1): 83–86.
65. W.H. Zachariasen. *Theory of X-ray Diffraction in Crystals*. Hoboken, NJ: John Wiley & Sons, 1945.
66. P.A. Rundquist, S. Jagannathan, R. Kesavamoorthy, C. Brnardic, S. Xu, S.A. Asher. "Photothermal Compression of Colloidal Crystals". *J. Chem. Phys.* 1991. 94(1): 711–717.
67. R. Kesavamoorthy, S. Jagannathan, P.A. Rundquist, S.A. Asher. "Colloidal Crystal Photothermal Dynamics". *J. Chem. Phys.* 1991. 94(7): 5172–5179.
68. Z. Hong, S.A. Asher. "Dependence of Raman and Resonance Raman Intensities on Sample Self-Absorption". *Appl. Spectrosc.* 2015. 69(1): 75–83.
69. Y.A. Gruzdkov, Y.M. Gupta. "Vibrational Properties and Structure of Pentaerythritol Tetranitrate". *J. Phys. Chem. A.* 2001. 105(25): 6197–6202.
70. W. Perger, J. Zhao, J. Winey, Y. Gupta. "First-Principles Study of Pentaerythritol Tetranitrate Single Crystals Under High Pressure: Vibrational Properties". *Chem. Phys. Lett.* 2006. 428(4): 394–399.
71. H. Tang, B. Torrie. "Raman Study of  $\text{NH}_4\text{NO}_3$  and  $\text{ND}_4\text{NO}_3$ -250-420 K". *J. Phys. Chem. Solids.* 1977. 38(2): 125–138.
72. M.R. Waterland, D. Stockwell, A.M. Kelley. "Symmetry Breaking Effects in  $\text{NO}_3^-$ : Raman Spectra of Nitrate Salts and Ab Initio Resonance Raman Spectra of Nitrate–Water Complexes". *J. Chem. Phys.* 2001. 114(14): 6249–6258.
73. J.M. Lightstone, T.B. Onasch, D. Imre, S. Oatis. "Deliquescence, Efflorescence, and Water Activity in Ammonium Nitrate and Mixed Ammonium Nitrate/Succinic Acid Microparticles". *J. Phys. Chem. A.* 2000. 104(41): 9337–9346.
74. C. Rodriguez-Nevarro, E. Doehne. "Salt Weathering: Influence of Evaporation Rate, Supersaturation and Crystallization Pattern". *Earth Surf. Proc. Land.* 1999. 24: 191–209.
75. W.J.P. van Enckevort, J.H. Los. "On the Creeping of Saturated Salt Solutions". *Cryst. Growth Des.* 2013. 13(5): 1838–1848.